MATERIALS CHEMISTRY FRONTIERS

CHINESE CHEMICAL SOCIETY

ROYAL SOCIETY OF CHEMISTRY

RESEARCH ARTICLE

View Article Online
View Journal | View Issue

Cite this: *Mater. Chem. Front.*, 2020, **4**, 1249

Fast-response/stable Ni–Bi cells achieved using hollowed-out Bi@carbon nanospheres: a preferred electricity storage choice to couple with clean energy harvesting†

Jiajia Yao,‡[a] Linpo Li,‡[b] Ning Li,[b] Jian Jiang,*[b] Yanlong Wang[c] and Jianhui Zhu*[a]

Received 13th January 2020,
Accepted 20th February 2020

DOI: 10.1039/d0qm00017e

rsc.li/frontiers-materials

Metallic bismuth (Bi) is a burgeoning choice of anode for rechargeable aqueous batteries given its large volumetric capacity, proper operating potential and highly reversible redox behavior. However, its further progress for full-cell implementation is unfortunately impeded due to the inferior anodic stability of Bi over long-term operation. Worse still, its low melting point (~271 °C) prevents the use of conventional optimizing techniques (*e.g.*, carbon modification) to alleviate tough anodic fading issues. We herein propose an unusual engineering protocol to enable Bi nanounits packaged into carbon sheaths using $NH_4Bi_3F_{10}$ nanospheres as initiating materials. Of particular note is that the high electrovalent bond of Bi–F plays a key role in promoting the bismuth thermal durability beyond 400 °C. Such Bi@carbon hybrids have special hollowed-out nanoscale features, with highly accessible surface areas, smooth ionic transport channels and robust mechanical properties against electrode degradation. The as-built anodes possess impressive specific capacity and rate capability (~53.9% capacity retention at 20 A g^{-1}), as well as prolonged cyclic lifespan (beyond 80% capacity retention after 10^3 cycles). More significantly, we further affirm the unique anodic phase conversions of "Bi ↔ $Bi(OH)_3$" on a real-time basis using characterizations/post-analysis at different cyclic stages. Our assembled Ni–Bi cells with notable peak energy/power densities of ~82.32 W h kg^{-1}/~15.7 kW kg^{-1} and fast-response and stable behavior, may be fit for green energy-harvesting use.

Growing concerns about environmental pollution and fossil fuel shortages have prompted the exploitation of green and sustainable energy alternatives (*e.g.*, solar, wind power, tide energy, *etc.*). Such natural energies are highly reliant on time, location and climate, and need to be firstly transferred into electricity and then instantly stored in rechargeable power devices.[1–3] In the past few decades, great effort has been devoted to Li/Na-ion batteries owing to their high output voltage and admirable energy densities. However, safety problems/risks induced by using flammable organic electrolytes, and limited elemental (*e.g.*, Li, Co) resources, make them far from satisfactory to meet the complex and irregular natural conditions, and grid-scale demands where achieving large specific energy is less critical than battery security.[4–6] As another historic and competitive category in the market, rechargeable batteries using highly ion-conducting and flame-retardant aqueous electrolytes are regarded as preferred collaborative candidates, benefiting from their salient merits of admirable power capability, low toxicity, affordable maintenance and operation costs, and reliable safety.[7–10] Many aqueous rechargeable battery (ARB) configurations have been implemented, like nickel–zinc (Ni–Zn),[11–13] zinc–manganese (Zn–Mn),[14,15] nickel–iron (Ni–Fe),[16–19] and nickel–bismuth (Ni–Bi),[20–22] *etc.* Among them, the emerging Ni–Bi batteries have triggered particular interest on account of the unique advantages from bismuthic anodes; including highly reversible redox reactions and reliable electrochemical potential range (−1.0–−0.2 V *vs.* SCE) wherein the hydrogen evolution reaction (HER) can be effectively suppressed or avoided in electrochemical phase conversions.[20–23] To date, despite numerous bismuth chalcogenides Bi_2X_3 (X = O, S, Se) being tried as feasible anodes for Ni–Bi cells, their common issues of, (i) poor intrinsic electrical conductivity and, (ii) inferior electrochemical

[a] *School of Physical Science and Technology, Southwest University, No. 2 Tiansheng Road, BeiBei District, Chongqing 400715, P. R. China. E-mail: jhzhu@swu.edu.cn*
[b] *School of Materials and Energy, Chongqing Key Lab for Advanced Materials and Technologies of Clean Energies, Southwest University, No. 2 Tiansheng Road, BeiBei District, Chongqing 400715, P. R. China. E-mail: jjiang@swu.edu.cn*
[c] *Key Laboratory of Chemical Lasers, Dalian Institute of Chemical Physics, Chinese Academy of Sciences, Dalian 116023, China*

† Electronic supplementary information (ESI) available: Experimental details. See DOI: 10.1039/d0qm00017e

‡ Jiajia Yao and Linpo Li contributed equally to this work.

stability (they tend to get pulverized even in a short cyclic period), cause retarded redox reaction kinetics and rapid electrode capacity decay merely after a few tens of cycles.[24–26]

Continual development of other feasible Bi-based anodes with superb physicochemical properties and desirable architectures has become indispensable for the advancement of Ni–Bi batteries. Metallic Bi might be an applicable anode choice given its superb electron-transfer capability, admirable electrochemical reactivity and excellent reversibility in distinct electrolytes, enabling a remarkable volumetric capacity of ~3765 mA h cm^{-3}.[24,27–29] These encouraging and optimal features encouraged us to develop "fast-response" and efficient ARBs to collect the intermittent electric energy. However, naked Bi anodes in bulk or nanoscale form inevitably suffer from severe structural pulverization and aggregation during repeated charge/discharge steps; these undesired structural instability problems lead to the rapid and drastic electrode capacity decay, which has been a major bottleneck for making long-cyclic Ni–Bi batteries.[29–31] Worse still, this short-cyclic issue can hardly be alleviated *via* conventional mechanical protection/reinforcement strategies (*e.g.*, carbon (C) coating *via* biomass carbonization), since their melting point is as low as ~271.3 °C.[24] That means Bi bulky metals can never be engineered directly *via* thermal approaches,[32,33] let alone the downsized Bi nanoparticles. This "inferior cyclability" problem for Bi activity without any robust protections, would persist owing to the structural instability in charge/discharge processes. To realize advanced bismuthic anodes with longer-term cyclic lifespans, putting each active nano Bi into an effective protective matrix *via* facile and scalable techniques is a key research area, but still remains a big challenge to date.

Herein, we intend to push forward Ni–Bi ARBs behavior using an anode of hollowed-out metallic Bi@C nanospheres that can be produced in large quantities *via* very facile and low-cost chemical treatment. The smart choice of multi-element $NH_4Bi_3F_{10}$ as the initiating precursor increases the structural durability of bismuthic species over 400 °C, thereby making it possible to put Bi nano-metals into the protective carbonaceous sheath matrix *via* thermal methods. Such a unique opened-up Bi@C nano-architecture would topologically ensure efficient electrode/electrolyte contact, and also provide enlarged active reaction sites and smooth inward/outward ionic transport channels. Note the exterior C sheath is mechanically robust to prevent the structural collapse of Bi caused by volume changes in repeated phase conversion processes. Also, such "metal-C" configured anodes are overall electrically conductive, in good support of the high-rate charge/discharge requirements for real applications. The aforementioned superiorities endow the electrode system with kinetically fast and stable anodic performance, capable of a specific capacity output of ~258.6 mA h g^{-1}, outstanding rate capability (retaining ~53.9% of its maximum capacity as the charge/discharge current rate jumps to 20 A g^{-1}), and superior cyclic durability (retaining ~80% capacity) over a 10^3 cycles. In addition, we further disclose the characteristic anodic phase conversions of "Bi ↔ $Bi(OH)_3$" and discuss their working mechanisms using modern *in situ* analysis at the distinct potentials. To verify their potential usage, we further construct full Ni–Bi ARB devices of (+)$CoNi_3O_4$@C//Bi@C(−), which can successfully achieve a maximum energy density of ~82.32 W h kg^{-1} and a maximum peak power density up to ~15.7 kW kg^{-1}, with a very low capacity decay rate (~0.028% per cycle) over a total of 10^3 cycles. This work presents a distinctive way to make reliable Bi@C anodes, which may guide new approaches to design other advanced electrodes that cannot be made by current thermal treatments.

The entire fabrication of the Bi@C nanosphere hybrids involves two main procedures, as shown schematically in Fig. 1a. The initial material, $NH_4Bi_3F_{10}$ nanoparticles, are prepared in large numbers in advance *via* a conventional liquid reaction process (by physically mixing A and B liquids at room temperature; see the Experimental details in the ESI†). After a simple centrifugal dissolution treatment, the homogenously mixed NH_4F and $Bi(NO_3)_3$ in ethylene glycol can instantly react with each other to form uniform $NH_4Bi_3F_{10}$ nanoparticles (JCPDS No. 48-0831; the corresponding X-ray diffraction (XRD) pattern is displayed in Fig. S1, ESI†):

$$10NH_4F + 3Bi(NO_3)_3 \rightarrow NH_4Bi_3F_{10} + 9NH_4NO_3$$

SEM (scanning electron microsopy) observations (Fig. 1b and c) evidently show all $NH_4Bi_3F_{10}$ nanospheres possess a smooth surface with a central diameter of ~50 nm. Step I is a general polymerization treatment for the $NH_4Bi_3F_{10}$ nanoparticles, which proceeds in a dopamine (DA; $C_8H_{11}O_2N$) Tris-buffer solution. Continual magnetic stirring enables the polymerization of DA molecules into polydopamine (PDA) layers (~5–10 nm in thickness), which are *in situ* and conformally grown on all exterior surfaces of the $NH_4Bi_3F_{10}$ precursors to yield the intermediate products of $NH_4Bi_3F_{10}$@PDA. The SEM image (Fig. 1d) reveals the highly dispersed $NH_4Bi_3F_{10}$@PDA nanoparticles still preserve the spherical geometric features except their diameter rises to an upper level of ~100 nm, suggesting the successful growth of

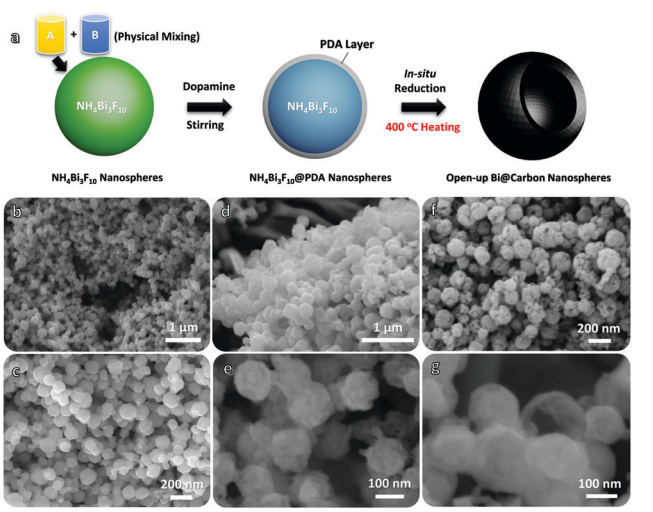

Fig. 1 (a) A schematic illustration of the synthesis of hollowed-out Bi@C nanospheres. (b–f) SEM observations of samples at distinct evolution stages: (b and c) pristine $NH_4Bi_3F_{10}$ nanospheres; (d and e) $NH_4Bi_3F_{10}$@PDA intermediates; (f and g) the final Bi@C hybrids.

PDA layers surrounding all the $NH_4Bi_3F_{10}$ cores. The zoomed-in SEM observation (Fig. 1e) uncovers that such hybrid nanospheres have rough and uneven surfaces where tiny nano-dots are distributed. This is highly associated with the *in situ* polymerization characteristics of DA molecules, which have a tendency to form either PDA conformal layers or nano-dots adhering to overall outer surfaces of foreign nanoparticles. Step II is an *in situ* thermal reduction procedure occurring under an Ar-filled atmosphere. The $NH_4Bi_3F_{10}$ decomposes into Bi nano-metals according to the following reactions:

$$NH_4Bi_3F_{10} \rightarrow NH_4F + 3BiF_3$$

$$xBiF_3 + 3C \rightarrow xBi + 3CF_x \quad (x = 1\text{–}4)$$

Fig. 1f and g reveal that the end-products of Bi@C hybrids are in a highly-dispersed physical state, and their spherical profiles are preserved as well; neither particle distortions nor aggregations are observed. Particularly noteworthy is that rather than pristine solid/sealed nanosphere constructions, each Bi@C nano-unit is mesoporous/opened-up, and has an intriguing and special "dissilient" configuration, whose structural formation may be caused by the loss of NH_3 and CF_x during annealing procedures.

The schematic in Fig. 2a vividly shows the potential advantages of such Bi@C hybrid products for ARB utilization. Our elaborately designed Bi@C hybrids have superior electrode construction over their solid/dense counterparts owing to the following aspects: first, metallic Bi (instead of conventional BiO_x) would better serve as an alternative electro-active substance due to its superb electrochemical reactivity for multi-electron redox reactions and excellent electrical conductivity. Second, the dissilient geometric morphology could supply more active reaction sites and shorten ion diffusion pathways in a cells' charge/discharge operation, endowing anodes with preferred electrode dynamics and fast rate behaviors. Third, the *in situ* evolved C sheath matrix can intimately wrap around Bi nanoparticles and keep them apart from each other, eventually acting as a robust "armour" that helps to buffer active volume changes and prevent severe particle aggregation in a long cyclic period. This may greatly promote the electrode durability. To elucidate their detailed structure characteristics and compositions, samples have been characterized thoroughly. The top-view SEM image (Fig. 2b) clearly shows that they have a spherical diameter ranging from ~50 to 100 nm in a highly dispersive/loose state in the absence of nanoparticle aggregation observations. The zoomed-in SEM image (Fig. 2c) further unveils that nearly all nanosphere units possess a geometrical "semi-opening" structure. The XRD record (Fig. 2d) shows that all emerging diffraction peaks are indexed to metallic bismuth (JCPDS No. 85-1329; $R\bar{3}m$(166), cell: 4.546 × 4.546 × 11.862 ⟨90.0 × 90.0 × 120.0⟩); and the absence of other possible impurities (*e.g.*, BiO_x, BiF_x) verifies the overall transformation of $NH_4Bi_3F_{10}$ into single-phased Bi nano-metals. The transmission electron microscopy (TEM) observations (Fig. 2e and Fig. S2, ESI†) confirm their special opened-up and intact nanostructures, where interesting valley-like channels appear at the central nanoparticle zone. This feature may offer sufficient room to buffer volume changes of active Bi and provide extra electrode–electrolyte interfaces for additional redox reactions. The contrast difference in Fig. 2e further implies their core–shell hybrid configurations. Fig. 2f and g successively display a typical high-resolution TEM image and a more close-up observation toward a selected region (marked in Fig. 2f). The spacing of the lattice fringes is measured to be ~0.33 nm, which corresponds well to the (012) plane of metallic Bi and agrees with the XRD analysis aforementioned. Note that an amorphous C layer (mean thickness: ~6 nm) is conformally encapsulated on the outer surface of the nanosized Bi. The ordered/bright diffraction spots in the selected area electron diffraction (SAED) pattern (see the inset in Fig. 2f) shows the hexagonal crystallinity nature of Bi.

The EDS spectrum (Fig. 2h) verifies the major presence of Bi and C elements in our hybrid products; the extra O signal mainly stems from PDA (–$[C_8H_{11}NO_2]$–n) evolved amorphous C (plenty of oxygen-related defects still exist), while the intensive Cu peak comes from the background. The EDS elemental mappings (Fig. S3, ESI†) visually affirms that the corresponding elements are evenly distributed in a large area; no additional elemental impurities are detected. High-resolution X-ray photoelectron spectroscopy (XPS) testing is used to disclose more chemical valence state information on Bi (Fig. 2i). Two individual fingerprint peaks lying at binding energies (BEs) of ~156.8 (Bi $4f_{7/2}$) and ~162.1 eV (Bi $4f_{5/2}$) (rather than in a higher scope of ~158.6–159.1 eV and ~163.8–164.7 eV for Bi^{3+} species) are fully consistent with Bi^0.[20,27] Furthermore, the N_2 adsorption/desorption measurement was performed to reflect the intrinsic porosity features of Bi@C nanospheres (Fig. 2j). The type-IV isotherm ensures the mesoporous nature of our samples (the major pore size is distributed in a narrow range of 2–20 nm), with a total specific surface area of ~97.3 $m^2\ g^{-1}$. Such characteristics may provide sufficient available sites for

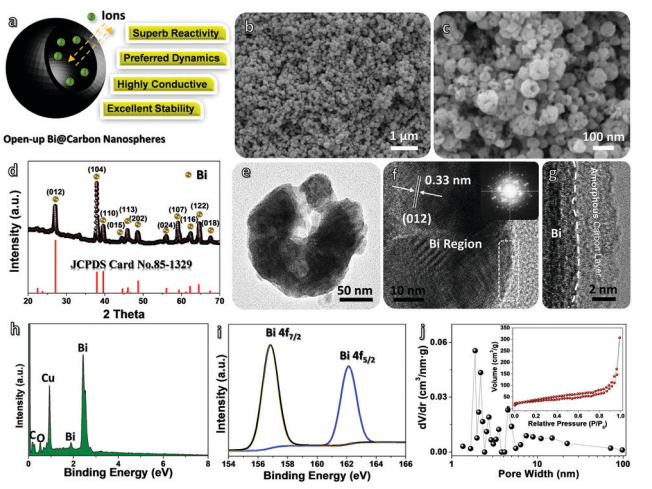

Fig. 2 (a) A schematic highlighting the potential advantages of Bi@C nanospheres. (b and c) SEM images, (d) XRD pattern, (e, f and g) TEM images, (h) EDS spectrum, (i) Bi 4f XPS spectrum, and (j) pore-size distribution plot for Bi@C hybrid samples. Insets in (f) and (j) show the SAED pattern and N_2 adsorption/desorption isotherm, respectively.

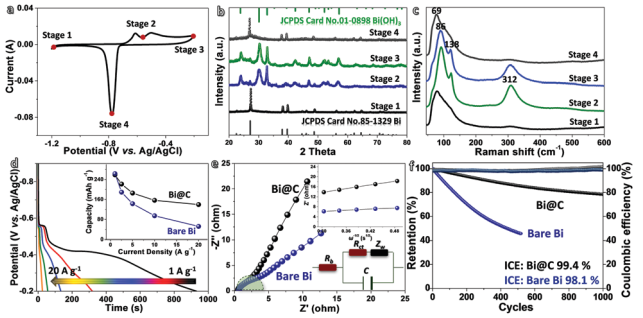

Fig. 3 Electrochemical testing of Bi@C nanospheres: (a) CV scan at 5 mV s^{-1}; *in situ* (b) XRD and (c) Raman spectroscopy; (d) galvanostatic discharge curves at distinct scan rates (inset: stored capacity as a function of current rate); (e) EIS spectrum (inset: the relationship between Z' and $\omega^{1/2}$ in a low-frequency region); (f) long-term cyclic record at 4 A g^{-1} (bare Bi nanoparticles are also evaluated for comparison).

efficient redox reactions together with convenient channels for fast ion diffusion.

A three-electrode testing system is initially set up to verify the electrochemical properties of the rationalized Bi@C samples. Fig. 3a shows its cyclic voltammetry (CV) curve at a scan rate of 5 mV s^{-1}. There are sharp anodic and cathodic peaks distinctly identified in a potential range of ~−1.2–0 V (*vs.* Ag/AgCl), declaring their highly reversible redox behaviors. In anodic scans, both typical peaks correspond to oxidation reactions starting from the metallic Bi^0, across possible intermediate Bi^+ (a metastable phase), and eventually to a chemical state of Bi^{3+} (in feasible forms of $Bi(OH)_3$, BiOOH or Bi_2O_3), due to disproportionation and other complex reactions as referred to in earlier classic literature:[11,20,34]

$$Bi^0 - e^- \leftrightarrow Bi^+$$

$$3Bi^+ \leftrightarrow 2Bi^0 + Bi^{3+}$$

$$Bi^{3+} + 3OH^- \leftrightarrow Bi(OH)_3 \leftrightarrow BiOOH + H_2O$$

or

$$2Bi^{3+} + 6OH^- \leftrightarrow Bi_2O_3 + 3H_2O$$

The sharp peak appearing at ~−0.50 V corresponds to a small fraction of active reaction sites located near the Bi metal–electrolyte interface, while the one at ~−0.61 V and the upper plateau may be associated with the in-depth oxidation of Bi bulk into Bi^{3+}-based products. The reverse cathodic scan involves a strong current peak at ~−0.78 V, which is closely related to a rapid three-electron reduction/deposition procedure from Bi^{3+} back to Bi^0. To get insight into the real-time chemical changes of Bi@C hybrids, *in situ* XRD probes are executed to identify their phase evolutions among distinct CV scanning stages (Fig. 3b). According to XRD pattern analysis, the original metallic Bi (marked as stage 1) is directly oxidized into $Bi(OH)_3$ (stage 2). This has been solidly evidenced by recorded diffraction signals, all of which come from $Bi(OH)_3$ (JCPDS Card No. 01-898) rather than other probable products like Bi^+, Bi^{2+} and Bi^{3+} species (*e.g.*, BiO, $Bi(OH)_2$, Bi_2O_3, *etc.*). This detection result is unlike the cases for micro-scale Bi electrodes (Bi ↔ Bi_2O_3).[20] Also, we can hardly find any diffraction signals from metastable Bi^+ substances. We believe that the fast reacting rate of nanosized Bi@C would disallow us to capture any direct evidence for soluble Bi^+ intermediates. Upon the increase in discharging depth (reaching −0.2 V *vs.* Ag/AgCl; stage 3), these present peaks still agree well with $Bi(OH)_3$. In reverse cathodic scans, the diffraction signals of $Bi(OH)_3$ are replaced by pristine peaks that are accurately indexed to Bi (JCPDS Card No. 85-1329), revealing the direct reversible phase conversion from $Bi(OH)_3$ back to metallic Bi (stage 4). Under the different charge/discharge status of Bi@C nanospheres, we also perform *in situ* Raman analyses (Fig. 3c; wavenumber range: 50–600 cm^{-1}), where the analysis keeps in line with our former XRD results and therefore affirms the reversible phase transitions between Bi^0 and Bi^{3+} during the charge/discharge cycles. The distinguishable Raman signals below the wavenumber of 200 cm^{-1} among all stages are mainly attributed to the superposition of distinct vibration modes (peak location: 69, 85 and 138 cm^{-1}) for bismuthic species (*e.g.*, Bi–Bi stretching or lattice vibrations); whereas, once electrodes are polarized at higher potentials (see stage 2 and 3), there is a broad peak emerging at 312 cm^{-1} that is assigned to a fingerprint peak for $Bi(OH)_3$. Based on the above discussion, the total reversible electrochemical reaction can be described below:

$$Bi + 3OH^- - 3e^- \leftrightarrow Bi(OH)_3$$

For comparison studies, the electrodes of bare Bi nanospheres are also tested. As noticed in the CV curves (see Fig. S4a, ESI†), both electrodes exhibit similar electrochemical features (governed by reversible reactions between Bi^0 and Bi^{3+}). Nevertheless, Bi@C electrodes exhibit a much stronger current signal, and a relatively lower peak separation value (~280 mV *vs.* ~420 mV) among the entire potential window, implying their enhanced charge-storage properties and better electrochemical kinetics. The CV plots of Bi@C electrodes under varied scan rates (from 5 to 40 mV s^{-1}) are displayed in Fig. S4b (ESI†). Along with the gradual rise of scan rates, neither a great peak shift nor CV profile deformation is present, suggesting fast reaction kinetics and superb electrochemical stability. Galvanostatic discharge curves at varied current densities (Fig. 3d) show that all discharge curves exhibit two well-defined potential plateaus situated at ~−0.62 and ~−0.51 V, highly consistent with our former CV analysis. According to discharge records, the stored specific capacities as a function of current rate are calculated and plotted in the inset of Fig. 3d. Compared with single Bi electrodes, Bi@C hybrid systems show the apparent capacity increase especially under high-rate current densities; when the current rate grows from 1 to 20 A g^{-1}, remarkable specific capacities varying from ~258.6 to ~139.4 mA h g^{-1} can be achieved, with an impressive capacity retention of ~53.9%. This is far superior to that of bare Bi (their capacities quickly drop to a level of ~46.1 mA h g^{-1}, with a poor capacity retention ratio of ~21%). To better elucidate these electrochemical properties, the electrochemical impedance

spectrum (EIS) analysis is conducted as well (see Fig. 3e; corresponding Nyquist plots and equivalent circuit model are involved). In the high-frequency range, Bi@C hybrid electrodes show a semicircle with a small fitting diameter of ~3.2 Ω, showing a lower charge-transfer resistance (R_{ct}) than bare Bi cases (R_{ct} value: ~4.5 Ω). The tail line at the low-frequency range reveals the Warburg impedance (Z_w) of electrodes, which is tightly associated with OH^- diffusion. The calculated ion diffusion coefficients for bare Bi and the Bi@C hybrid (calculation details are available in the ESI†) are 3.20×10^{-13} and 3.43×10^{-12} cm^2 s^{-1}, respectively. Note that Bi@C hybrids have a larger ionic diffusion coefficient (almost one order of magnitude higher than that of bare Bi anodes). This preferred electrochemical behavior might be attributed to their unique opened-up architecture (capable of shortening the OH^- diffusion length in the solid phase) and loosened structures (made by C atom etching under thermal conditions).

The cyclic stability is usually considered to be a major obstacle impeding the practical progress of bismuthic anodes. We hence evaluate the deep cyclic performance of Bi@C hybrids *via* continuous charge/discharge measurements at a constant current density of 4 A g^{-1} (Fig. 3f). To highlight their long-lasting cyclic durability, bare Bi electrodes are also measured in parallel. The coulombic efficiency (CE) values of pre-activated Bi@C and Bi electrodes are both close to 100% among the whole cyclic process (initial CE: 99.4% for Bi@C; 98.1% for bare Bi), reflecting the good electrode reversibility among the overall cyclic operation. Note that Bi@C electrodes possess prominent cyclic behavior, with more than 80% capacity retention after 10^3 cycles. By sharp contrast, the specific capacity of naked Bi counterparts fades quickly from the onset cycling, with less than 55% capacity survival after a mere 500 cycles. This result unquestionably confirms the electrochemical superiority of the smart combination and integration of high-reactivity Bi and stable C sheaths. Typical SEM (Fig. S5a, ESI†) and TEM images of cycled Bi@C electrodes reveal that there are no great changes in their particle size/overall morphology, though some of them suffer from damage or collapse, as implied by the presence of debris (Fig. S5b and c, ESI†). The SAED pattern (Fig. S5d, ESI†) indicates the polycrystalline/near-amorphous features of the cycled electrodes.

To prove the feasibility of their utilization in ARBs, a full-cell system has been built using $CoNi_3O_4$@C nanowall arrays (NWAs; see their basic characterization and half-cell behavior in Fig. S6 and S7, ESI†) as the cathode to pair with our anode (denoted as (+)$CoNi_3O_4$@C//Bi@C(−)). Fig. 4a displays the schematic of the detailed cell configuration. The choice of $CoNi_3O_4$@C NWAs as the counter electrode is because of its superb and fast-response Faradaic behavior for energy-storage utilization. To balance the stored charges in assembled Ni–Bi batteries, the mass ratio of Bi@C and $CoNi_3O_4$@C has been set by referring to their respective CV plots (Fig. S8, ESI†). Fig. 4b presents the CV curve of optimized Ni–Bi ARBs within a potential window of 0–1.4 V at a scan rate of 5 mV s^{-1}. The CV profile shows the electrochemical characteristics of both the anode and cathode well, accompanied by two oxidation peaks at ~0.95 and ~1.16 V as well as one reduction peak at ~0.78 V,

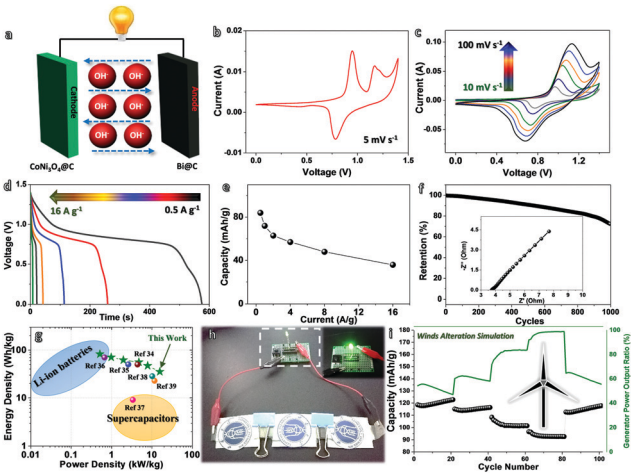

Fig. 4 (a) A schematic showing the full-cell device configuration. (b) Typical CV scan at 5 mV s^{-1}, (c) CV plots and (d) galvanostatic discharge profiles at varied scan rates, (e) stored capacity as a function of current rate, (f) long-term cyclic record at 4 A g^{-1}, and the EIS spectrum (inset), (g) Ragone plot of our full-cell device. (h) An photo showing that three serially connected cells can light up a green LED indicator. (i) Corresponding dynamic response plot of the assembled cells under a wind alternative simulation program.

which may be ascribed to the overall electrochemical reaction of:

$$CoNi_3O_4 + Bi + 7OH^- - 7e^- \leftrightarrow CoOOH + 3NiOOH + Bi(OH)_3$$

The CV curves of the full-cell device under various scan rates are depicted in Fig. 4c. Upon increasing scan rates, two oxidation peaks merge together to form one well-defined and strong peak located at ~1.1 V, while the reduction peak is still lying at ~0.70 V. Except for a slight peak position shift, there are no evident CV profile deformations/distortions appearing, confirming the fast charge/discharge behavior of our Ni–Bi ARBs. The cell performance is further measured by galvanostatic testing, and the corresponding discharge profiles at distinct current rates from 0.5 to 16 A g^{-1} are plotted in Fig. 4d. All discharge curves demonstrate a characteristic plateau near ~0.85 V; no evident IR drops are detected with the rise of current rates. The cell capacity is then calculated and plotted as a function of current density (Fig. 4e). At a small current rate of 0.5 A g^{-1} (charge/discharge time: tens of mins), the assembled Ni–Bi cells can deliver a maximum specific capacity of ~84.5 mA h g^{-1}. Once the current density grows to a high level of 16 A g^{-1} (32 times the initial current value; the cell charge/discharge finishes in few seconds), cells still retain a total capacity close to ~40 mA h g^{-1} (~47.3% of the maximum value). The "supercapacitor"-like charge/discharge features highly reflect the prominent reaction kinetics and superior rate performance of (+)$CoNi_3O_4$@C//Bi@C(−) cells. The long-term cyclic stability of our batteries is then measured under a constant current rate of 4 A g^{-1} (Fig. 4f), capable of exhibiting a high capacity retention of ~72.4% after 10^3 cycles. The Nyquist plot in the inset of Fig. 4f shows a low R_s value (~3.8 Ω) together with a very tiny R_{ct} (~0.6 Ω) in the assembled full-cell systems,

ensuring their fast charge-transfer properties. The inclined line with an angle of $\sim 45^{\circ}$ in the low-frequency region indicates the expedited ion-diffusion features.

Fig. 4g shows the Ragone plot of (+)$CoNi_3O_4$@C//Bi@C(−) cells, uncovering the significant specific energy/power information for practical battery usage (maximum energy density: ~ 82.32 W h kg^{-1} at ~ 0.44 kW kg^{-1}; maximum power density: ~ 15.7 kW kg^{-1}). Notably, their maximum power parameters even outperform those of many classic ARBs or asymmetric/hybrid supercapacitors (*e.g.*, CC/CNF/Ni-Co//LDH-CC/CNF/Bi_2O_3, 4.4 kW kg^{-1}; $Ni(OH)_2$/GS//Bi_2O_3/GS, 2.6 kW kg^{-1}; $Ni(OH)_2$//$BiO_4CO_3(OH)_2$, 0.67 kW kg^{-1}; Bi_2O_3//MnO_2, 3.37 kW kg^{-1}; FeOOH//Co–Ni LDH, 11.6 kW kg^{-1}; $NiMoO_4$//FeOOH HSC, 10.94 kW kg^{-1}).[35–41] This confirms the ultrafast charge/discharge capability and remarkable energy-storage behavior of our assembled cell, which may bridge the gap between batteries and supercapacitors. Fig. 4h shows a high-power LED indicator (color: green; turn-on voltage: ~ 2.4 V) can be readily lit by three serially-connected cells, and kept working for dozens of minutes. To further evidence the great potential in coordination with clean energy (like wind energy) collection under variable environmental conditions (*e.g.*, varied wind speed/strength), we have purposely simulated wind alternation by programming the electricity input/output procedures, and evaluated the dynamic response of our (+)$CoNi_3O_4$@C//Bi@C(−) cells (See Fig. 4i). As recorded, such cells could couple synchronously with external wind power even if the wind speed suddenly changes a lot, which may hold great promise in real applications for green energy harvesting.

In summary, an intriguing opened-up Bi@C nanosphere hybrid was constructed as a novel anode for ultrafast and stable Ni–Bi ARBs. The well-designed Bi@C composite integrated the features of ultrafast charge transfer, smooth ionic diffusion, a sufficient electrode–electrolyte contact interface and excellent structural stability. Thanks to these advantages, the as-prepared Bi@C hybrid exhibits outstanding rate capability with 53.9% capacity retention at an ultrahigh current rate of 20 A g^{-1}, and prominent cyclic performance capable of retaining $\sim 80\%$ capacity after 10^3 continual cycles. As a demonstration of their function in real applications, an ARB, (+)$CoNi_3O_4$@C//Bi@C(−), was developed. A considerable energy density of ~ 82.32 W h kg^{-1} together with a peak power density of ~ 15.7 kW kg^{-1} can be achieved in the activated Ni–Bi ARBs, which may bridge the gap between supercapacitors and batteries, and therefore exert important practical significance for energy-storage devices. Additionally, the full Ni–Bi ARBs show prominent long-term cyclic performance, retaining $\sim 72.4\%$ capacity after 10^3 cycles. Our work may not only supply a smart and economical way to realize intriguing Bi@C hybrid configurations for ARB applications, but also prove their fast-response and stable behavior can be coupled with green energy harvesting.

Conflicts of interest

There are no conflicts to declare.

Acknowledgements

This work is supported by grants from the National Natural Science Foundation of China (51802269), the Chongqing Natural Science Foundation (cstc2018jcyjAX0624), the Fundamental Research Funds for the Central Universities (XDJK2020D034, XDJK2019AA002), and the Venture & Innovation Support Program for Chongqing Overseas Returnees (cx2018027).

References

1 D. Larcher and J.-M. Tarascon, Towards greener and more sustainable batteries for electrical energy storage, *Nat. Chem.*, 2015, **7**, 19.
2 J. Jiang, Y. Li, J. Liu, X. Huang, C. Yuan and X. W. Lou, Recent advances in metal oxide-based electrode architecture design for electrochemical energy storage, *Adv. Mater.*, 2012, **24**, 5166.
3 W. Zuo, R. Li, C. Zhou, Y. Li, J. Xia and J. Liu, Battery-supercapacitor hybrid devices: recent progress and future prospects, *Adv. Sci.*, 2017, **4**, 1600539.
4 J. F. Parker, C. N. Chervin, I. R. Pala, M. Machler, M. F. Burz, J. W. Long and D. R. Rolison, Rechargeable nickel–3D zinc batteries: An energy-dense, safer alternative to lithium-ion, *Science*, 2017, **356**, 415.
5 D. Kundu, B. D. Adams, V. Duffort, S. H. Vajargah and L. F. Nazar, A high-capacity and long-life aqueous rechargeable zinc battery using a metal oxide intercalation cathode, *Nat. Energy*, 2016, **1**, 16119.
6 J. Liu, C. Xu, H. Jiang, C. Li, L. Zhang, J. Lin and Z. X. Shen, Advanced energy storage devices: basic principles, analytical methods, and rational materials design, *Adv. Sci.*, 2018, **5**, 1700322.
7 H. Kim, J. Hong, K.-Y. Park, H. Kim, S.-W. Kim and K. Kang, Aqueous rechargeable Li and Na ion batteries, *Chem. Rev.*, 2014, **114**, 11788.
8 M. Gong, Y. Li, H. Zhang, B. Zhang, W. Zhou, J. Feng, H. Wang, Y. Liang, Z. Fan, J. Liu and H. Dai, Ultrafast high-capacity NiZn battery with NiAlCo-layered double hydroxide, *Energy Environ. Sci.*, 2014, **7**, 2025.
9 J. Jiang, Y. Liu, L. Li, J. Zhu, M. Xu and C. M. Li, Smart magnetic interaction promotes efficient and green production of high-quality Fe_3O_4@Carbon nanoactives for sustainable aqueous batteries, *ACS Sustainable Chem. Eng.*, 2018, **6**, 757.
10 H. Pan, Y. Shao, P. Yan, Y. Cheng, K. S. Han, Z. Nie, C. Wang, J. Yang, X. Li, P. Bhattacharya, K. T. Mueller and J. Liu, Reversible aqueous zinc/manganese oxide energy storage from conversion reactions, *Nat. Energy*, 2016, **1**, 16039.
11 J. Liu, C. Guan, C. Zhou, Z. Fan, Q. Ke, G. Zhang, C. Liu and J. Wang, A flexible quasi-solid-state nickel–zinc battery with high energy and power densities based on 3D electrode design, *Adv. Mater.*, 2016, **28**, 8732.
12 C. Xu, J. Liao, C. Yang, R. Wang, D. Wu, P. Zou, Z. Lin, B. Li, F. Kang and C.-F. Wong, An ultrafast, high capacity and superior longevity Ni/Zn battery constructed on nickel nanowire array film, *Nano Energy*, 2016, **30**, 900.
13 P. Hu, T. Wang, J. Zhao, C. Zhang, J. Ma, H. Du, X. Wang and G. Cui, Ultrafast alkaline Ni/Zn battery based on

Bi-foam-supported Ni_3S_2 nanosheets, *ACS Appl. Mater. Interfaces*, 2015, **7**, 26396.

14 N. Zhang, F. Cheng, J. Liu, L. Wang, X. Long, X. Liu, F. Li and J. Chen, Rechargeable aqueous zinc–manganese dioxide batteries with high energy and power densities, *Nat. Commun.*, 2017, **8**, 405.

15 L. Ma, L. Li, Y. Liu, J. Zhu, T. Meng, H. Zhang, J. Jiang and C. M. Li, Building better rechargeable Zn–Mn batteries with a highly active Mn_3O_4/carbon nanowire cathode and neutral Na_2SO_4/$MnSO_4$ electrolyte, *Chem. Commun.*, 2018, **54**, 10835.

16 C. Guan, W. Zhao, Y. Hu, Q. Ke, X. Li, H. Zhang and J. Wang, High-Performance flexible solid-state Ni/Fe battery consisting of metal oxides coated carbon cloth/carbon nanofiber electrodes, *Adv. Energy Mater.*, 2016, **6**, 1601034.

17 J. Liu, M. Chen, L. Zhang, J. Jiang, J. Yan, Y. Huang, J. Lin, H. J. Fan and Z. X. Shen, A flexible alkaline rechargeable Ni/Fe battery based on graphene foam/carbon nanotubes hybrid film, *Nano Lett.*, 2014, **14**, 7180.

18 H. Wang, Y. Liang, M. Gong, Y. Li, W. Chang, T. Mefford, J. Zhou, J. Wang, T. Regier, F. Wei and H. Dai, An ultrafast nickel–iron battery from strongly coupled inorganic nanoparticle/nanocarbon hybrid materials, *Nat. Commun.*, 2012, **3**, 917.

19 L. Li, J. Zhu, Y. Niu, Z. Xiong and J. Jiang, Metallic Fe nanoparticles trapped in self-adapting nanoreactors: a novel high-capacity anode for aqueous Ni–Fe batteries, *Chem. Commun.*, 2017, **53**, 12661.

20 Y. Zeng, Z. Lin, Y. Meng, Y. Wang, M. Yu, X. Lu and Y. Tong, Flexible ultrafast aqueous rechargeable Ni//Bi battery based on highly durable single-crystalline bismuth nanostructured anode, *Adv. Mater.*, 2016, **28**, 9188.

21 P. Zhang, Y. Zeng, M. Wang, W. Xu, Y. Liu and X. Lu, A highly crystalline bismuth superstructure for ultrastable and high-performance flexible aqueous nickel–bismuth batteries, *J. Mater. Chem. A*, 2015, **6**, 8895.

22 Y. Zeng, Z. Lin, Z. Wang, M. Wu, Y. Tong and X. Lu, *In situ* activation of 3D porous Bi/carbon architectures: toward High-energy and stable nickel–bismuth batteries, *Adv. Mater.*, 2018, **30**, 1707290.

23 W. Zuo, W. Zhu, D. Zhao, Y. Sun, Y. Li, J. Liu and X. W. Lou, Bismuth oxide: a versatile high-capacity electrode material for rechargeable aqueous metal-ion batteries, *Energy Environ. Sci.*, 2016, **9**, 2881.

24 J. Ni, X. Bi, Y. Jiang, L. Li and J. Lu, Bismuth chalcogenide compounds Bi_2X_3 (X = O, S, Se): Applications in electrochemical energy storage, *Nano Energy*, 2017, **34**, 356.

25 Y. Li, M. A. Trujill, E. Fu, B. Patterson, L. Fei, Y. Xu, S. Deng, S. Smimov and H. Luo, Bismuth oxide: a new lithium-ion battery anode, *J. Mater. Chem. A*, 2013, **1**, 12123.

26 J. Ni, Y. Zhao, T. Liu, H. Zheng, L. Gao, C. Yan and L. Li, Strongly coupled Bi_2S_3@CNT hybrids for robust lithium storage, *Adv. Energy Mater.*, 2014, **4**, 1400798.

27 C.-F. Sun, J. Hu, P. Wang, X.-Y. Cheng and S. B. Lee, Li_3PO_4 matrix enables a long cycle life and high energy efficiency bismuth-based battery, *Nano Lett.*, 2016, **16**, 5875.

28 C. Park, S. Yoon, S. Lee and H. Sohn, Enhanced electrochemical properties of nanostructured bismuth-based composites for rechargeable lithium batteries, *J. Power Sources*, 2009, **186**, 206.

29 J. Chen, X. Fan, X. Ji, T. Gao, X. Zhou, L. Wang, F. Wang, C. Yang, L. Chen and C. S. Wang, Intercalation of Bi nanoparticles into graphite results in an ultra-fast and ultra-stable anode material for sodium-ion batteries, *Energy Environ. Sci.*, 2018, **11**, 1218.

30 K. Gopalsamy, Z. Xu, B. Zheng, T. Huang, L. Kou, X. Zhao and C. Gao, Bismuth oxide nanotubes–graphene fiber-based flexible supercapacitors, *Nanoscale*, 2014, **6**, 8595.

31 J. Wang, H. Zhang, R. C. Hunt, A. Charles, J. Tang, O. Bretcanu, D. Walker, K. T. Hassan, Y. Sun and L. Šiller, Synthesis and characterisation of reduced graphene oxide/bismuth composite for electrodes in electrochemical energy storage devices, *ChemSusChem*, 2017, **10**, 363.

32 R. Li, Y. Wang, C. Zhou, C. Wang, X. Ba, Y. Li, X. Huang and J. Liu, Carbon-stabilized high-capacity ferroferric oxide nanorod array for flexible solid-state alkaline battery–supercapacitor hybrid device with high environmental suitability, *Adv. Funct. Mater.*, 2015, **25**, 5384.

33 C. Guan, J. Liu, Y. Wang, L. Mao, Z. Fan, Z. Shen, H. Zhang and J. Wang, Iron oxide-decorated carbon for supercapacitor anodes with ultrahigh energy density and outstanding cycling stability, *ACS Nano*, 2015, **9**, 5198.

34 V. Vivier, A. Regis, G. Sagon, J.-Y. Nedelec, L. T. Yu and C. C. Vivier, Cyclic voltammetry study of bismuth oxide Bi_2O_3 powder by means of a cavity microelectrode coupled with Raman microspectrometry, *Electrochim. Acta*, 2001, **46**, 907.

35 X. Li, C. Guan, Y. Hu and J. Wang, Nanoflakes of Ni–Co LDH and Bi_2O_3 assembled in 3D carbon fiber network for high-performance aqueous rechargeable Ni/Bi battery, *ACS Appl. Mater. Interfaces*, 2017, **9**, 26008.

36 J. Sun, Z. Li, J. Wang, W. Hong, P. Gong, P. Wen, Z. Wang and S. Yang, Ni/Bi battery based on $Ni(OH)_2$ nanoparticles/graphene sheets and Bi_2O_3 rods/graphene sheets with high performance, *J. Alloys Compd.*, 2015, **643**, 231.

37 J. Sun, J. Wang, Z. Li, L. Niu, W. Hong and S. Yang, Assembly and electrochemical properties of novel alkaline rechargeable Ni/Bi battery using $Ni(OH)_2$ and $(BiO)_4CO_3(OH)_2$ microspheres as electrode materials., *J. Power Sources*, 2015, **274**, 1070.

38 H. Xu, X. Hu, H. Yang, Y. Sun, C. Hu and Y. Huang, Flexible asymmetric micro-supercapacitors based on Bi_2O_3 and MnO_2 nanoflowers: larger areal mass promises higher energy density, *Adv. Energy Mater.*, 2014, **5**, 1401882.

39 J. Chen, J. Xu, S. Zhou, N. Zhao and C. P. Wong, Amorphous nanostructured FeOOH and Co–Ni double hydroxides for high-performance aqueous asymmetric supercapacitors, *Nano Energy*, 2016, **21**, 145.

40 K. A. Owusu, L. Qu, J. Li, Z. Wang, K. Zhao, C. Yang, K. M. Hercule, C. Li, C. Shi, Q. Wei, L. Zhou and L. Q. Mai, Low-crystalline iron oxide hydroxide nanoparticle anode for high-performance supercapacitors, *Nat. Commun.*, 2016, **8**, 14264.

41 J. Zhu, J. Jiang, Z. Sun, J. Luo, Z. Fan, X. Huang, H. Zhang and T. Yu, 3D carbon/cobalt-nickel mixed-oxide hybrid nanostructured arrays for asymmetric supercapacitors, *Small*, 2014, **10**, 2937.